A Type-I van der Waals Heterobilayer of $WSe_2/MoTe_2$

Ming Li[1], Matthew Z. Bellus[3], Jun Dai[2], Liang Ma[2] Xiuling Li[2], Hui Zhao[3*] & Xiao Cheng Zeng[2]*

[1]College of Chemical engineering, Hebei Key Laboratory for Environment Photocatalytic and Electrocatalytic Materials, North China University of Science and Technology, Tang Shan, Hebei 063000, China
[2]Department of Chemistry, University of Nebraska-Lincoln, Lincoln, NE 68588, USA
[3]Department of Physics and Astronomy, the University of Kansas, Lawrence, Kansas 66045, USA

E-mail: *Corresponding Authors, xzeng1@unl.edu; huizhao@ku.edu

17 May 2018

Abstract.

We present a joint theoretical/experimental study of a van der Waals heterobilayer with type-I band alignment formed by monolayers of WSe_2 and $MoTe_2$. Our first-principles computation suggests that both the valence band maximum and the conduction band minimum of the $WSe_2/MoTe_2$ heterobilayer reside in the $MoTe_2$ layer. The type-I band alignment allows efficient transfer of excitons from WSe_2 to $MoTe_2$. Since monolayer $MoTe_2$ is a direct semiconductor with a bandgap in the infrared range, this heterobilayer is attractive for infrared light emission applications. Time-resolved measurements of photocarrier dynamics were conducted to provide experimental evidence of the type-I nature of this heterobilayer. In these measurements, we found that excitation energy can transfer from WSe_2 to $MoTe_2$ efficiently, but not along the opposite direction. The efficient energy transfer can serve as an optical gain or wavelength conversion mechanism for efficient emission from $MoTe_2$, which can be utilized in ultrathin and efficient infrared light sources.

Keywords: van der Waals heterostructure, type-I band alignment, two-dimensional material, ultrafast dynamics

Submitted to: *Nanotechnology*

1. Introduction

The emergence of semiconductor heterostructures has resulted in remarkable progress in modern semiconductor technology. A large family of semiconductor heterostructure

devices have been industrialized and widely used in many areas, such as efficient double-heterostructure light-emitting diodes and laser-based telecommunication systems, bipolar transistors, solar cells, as well as high-electron-mobility transistors [1, 2]. From a fundamental point of view, the behavior of a semiconductor heterostructure crucially depends on the band alignment at the interface. According to the band offset at the interface, three types of band alignments can be formed: straddling gap (type-I), staggered gap (type-II) or broken gap (type-III) (see Figure S1, supplementary material).

For straddling (type-I) offset heterojunctions, the conduction band minimum (CBM) and the valence band maximum (VBM) are located at the same side of the heterointerface. As an ideal lattice-matched type-I heterostructure, GaAlAs/GaAs was proposed in 1967 by Alferov [1, 2]. Since then, this heterostructure has been widely used for applications of rooted in wavelength conversion or optical pumping like semiconducting lasers and quantum-well structures. Owing to the rapid development of heterostructure growth techniques in the 1970s, such as molecular-beam epitaxy and metal organic chemical vapor deposition technologies, many new heterostructures can be realized now. For staggered offset (type-II) heterojunctions, electrons and holes are spatially separated and localized in self-consistent potential wells at different sides of the heterointerface, a feature good for the tunability of their peculiarities. Type-II heterojunctions have drawn little attention in the past until Kroemer demonstrated its operating principle and provided several semiconductor combinations that exhibit the staggered lineup [3]. Since then, increasing number of new type-II heterostructures were investigated as functional semiconductors.

Recently, much research attention has been devoted to heterostructures composed of two-dimensional (2D) materials. In contrast to epitaxially grown traditional heterostructures, 2D layered materials in 2D heterostructures are stacked mechanically along the direction perpendicular to the 2D plane *via* van der Waals interactions [4]. Among 2D materials, transition metal dichalcogenides (TMDCs, MX_2) are of particular interest due to their tunable electronic and optical properties [5]. Despite their relatively weak interlayer adhesion, heterostructures formed by TMDCs have shown strong interlayer coupling, which facilitates fast and efficient interlayer charge transfer [6, 7]. In addition, these materials possess other properties desirable for various applications, such as mechanical flexibility, atomically sharp interfaces, and the ability to stack different materials without much concern for lattice mismatching.

Most of the van der Waals heterostructures that have been realized experimentally, consisting primarily of combinations of MoS_2, $MoSe_2$, WS_2 and WSe_2, have exhibited type-II band alignment. Several promising applications have been proposed based on these type-II heterostructures, such as ultrathin solar cells with high power densities, and vertical tunneling transistors with low power consumption [8], photocatalysis [9], and other optoelectronic applications [10]. Although these heterostructures possess many exciting features for applications, the ability to utilize type-I 2D layered structures is expeced to create a new direction for bandstructure engineering in ultrathin structures and to realize new applications for the van der Waals heterostructure family. Recently,

band offsets of TMDCs have been studied by employing first-principles calculations [11, 12, 13]. Nevertheless, there was a scarcity of realized type-I TMDC heterostructures. Since in type-I heterostructures both electrons and holes reside in one material, their radiate recombination is enhanced. Hence, type-I heterostructures are attractive for light-emitting applications. Furthermore, introducing new type-I heterostructures can expand the heterointerface library for future development of multilayer structures with sophisticated landscapes of band alignment.

Here we report a theoretical and experimental study of a van der Waals heterobilayer with type-I band alignment formed by monolayers of WSe_2 and $MoTe_2$. Our first-principles computation suggests that both the CBM and the VBM of the $WSe_2/MoTe_2$ heterobilayer reside in $MoTe_2$. Time-resolved pump-probe measurements of photocarrier dynamics provide evidence of the type-I nature of this heterobilayer. We found that excitation energy can transfer from WSe_2 to $MoTe_2$, but not along the opposite direction. The efficient energy transfer can serve as an optical gain or wavelength conversion mechanism for efficient emission from $MoTe_2$. Since monolayer $MoTe_2$ is a direct semiconductor with a bandgap in the infrared range, this heterobilayer is attractive for infrared light emission applications.

2. Computational Methods

All computations were carried out within the density functional theory (DFT) framework by using the Vienna *ab initio* simulation package, VASP 5.3 [14]. The generalized gradient approximation (GGA) in the form of Becke86 was adopted for exchange-correlation functional [15]. Furthermore, the optB86b-vdW functional was used for structure optimization to account for the weak interlayer van der Waals interactions [16]. The interaction between the core electrons and valence electrons was modeled by the projector augmented wave method [17]. It is known that GGA functional tends to underestimate the bandgap of semiconductors. So the electronic structures were computed using the Heyd-Scuseria-Ernzerhof (HSE06) hybrid functional in company with the optB86b-vdW functional for structure relaxation [18]. Energy cutoff for the plane-wave expansion was set to 500 eV. Brillouin zone sampling was performed with Monkhorst-Pack (MP) special k-point meshes. The 2D Brillouin zone integration using the Γ-center scheme was sampled with a $9 \times 9 \times 1$ grid for MX_2. A vacuum layer greater than 20 Åwas taken so that the interaction between adjacent images can be neglected. All atoms were allowed to relax during the geometry optimization until the computed Hellmann-Feynman force on each atom was smaller than 0.01 eV/Å. The convergence threshold was set as 10^{-5} eV in energy for optB86-vdW functional based structure optimization. For the bandstructure computations, the Brillouin zone of Γ-K-M-Γ is selected for monolayer MX_2 [12, 19]. Spin-orbit coupling (SOC) was included in optB86-vdW as well as HSE06 functional based calculations. Moreover, the band structures computed without SOC were also presented for comparison. For computing the partial density of states (PDOS) of the $MoTe_2/WSe_2$ heterobilayer (54 units of

$MoTe_2$ and 62 units of WSe_2), the 2D Brillouin zone integration using the Γ-center scheme was sampled with a $5 \times 5 \times 1$ grid.

3. Experimental Methods

The $WSe_2/MoTe_2$ heterobilayer sample was fabricated by mechanically exfoliating monolayers of WSe_2 and $MoTe_2$ onto polydimethylsiloxane (PDMS) substrates and sequentially transferring the layers to a Si/SiO_2 (90 nm) substrate. The monolayer thickness of the flakes were determined by their reflective contrast on transparent PDMS substrates [20, 21]. Due to the relative instability of $MoTe_2$ monolayer in ambient conditions, this layer was completely covered by the WSe_2 monolayer, in order to increase the longevity of the heterobilayer sample. Isolated monolayer regions of both materials were also present on the same substrate, which facilitates their direct comparison with the heterobilayer. The uncovered $MoTe_2$ monolayers typically degrade in a few days under ambient conditions. The sample was annealed for 2 hours at 200°C in a H_2/Ar (5 sccm/100 sccm) environment at a base pressure of about 3 torr.

To study photocarrier dynamics in the heterobilayer, we employed a transient absorption technique in reflection geometry [22]. In these measurements, a tightly focused pump pulse of about 100 fs duration was used to excite certain regions of the sample, which could be the heterobilayer, WSe_2 monolayer, or $MoTe_2$ monolayer. Then, a probe pulse, which arrives at the sample after the pump and overlaps in space with the pump spot, was used to monitor the dynamics of the photocarriers. The differential reflection of the probe, $\Delta R/R_0 = (R - R_0)/R_0$, is measured as a function of the relative time delay between two pulses, defined as the probe delay. Here, R and R_0 represent the reflection of the probe pulse by the sample with and without the presence of the pump pulse, respectively. By choosing the pump photon energies, we can preferentially inject photocarriers in different layers of the heterobilayer sample. Similarly, by tuning the probe photon energy to resonate with a certain layer, we can selectively probe population of carriers in that layer, based on the fact that the differential reflection signal is proportional to the carrier density [22]. All the measurements were performed with the sample under ambient conditions.

4. Results and Discussion

4.1. Computational results

The most stable phase of TMDC monolayers was considered in this study. It has been demonstrated that ReS_2 and $ReSe_2$ have a distorted $CdCl_2$-type structure (the $1T$ phase) [21, 23]. For other TMDCs (MX_2, M = Cr, Mo, W; X = S, Se, Te), the most stable structure is the $2H$ phase. As shown in Table S1 (see supplementary material), the optimized lattice constants based on the optB86b-vdW functional agree well with previous calculations [11, 12, 24, 25, 26]. The computed bandgaps of MX_2 monolayers based on the optB86b-vdW and HSE06 functionals with SOC

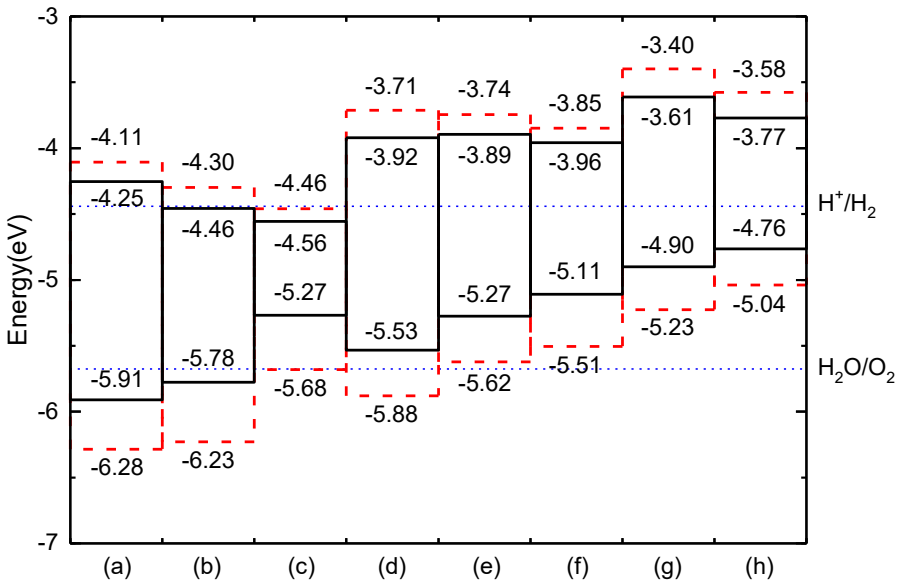

Figure 1. Computed band alignment of MX_2 monolayers: (a) MoS_2, (b) ReS_2, (c) $CrSe_2$, (d) WS_2, (e) $MoSe_2$, (f) $ReSe_2$, (g) WSe_2, and (h) $MoTe_2$. The black solid lines show the optB86b-vdW results. The red dashed lines denote the HSE06+SOC results. The blue dotted lines indicate the water reduction (H^+/H_2) and oxidation (H_2O/O_2) potentials. The vacuum level is set to zero

are in reasonable agreement with the experimental values and previous theoretical results[27, 28, 29, 30, 31, 32, 33, 34, 35, 36, 37, 38, 39, 40].

Figure 1 shows the band alignments of monolayer MX_2 (M = Cr, Mo, W, Re; X = S, Se, Te) obtained based on optB86b-vdW and HSE06+SOC computations. Several general trends can be identified. The optB86b-vdW results are discussed as follows: For MoX_2, WX_2, and ReX_2 (X = S, Se), the VBM and CBM of MX_2 increase monotonously with the atomic number of element X. Thus, $MoS_2/MoSe_2$, WS_2/WSe_2, and $ReS_2/ReSe_2$ heterobilayers are more likely to exhibit type-II band alignments. Moreover, the VBM and CBM of MoX_2 (X = S, Se) are lower than those of WX_2. Hence, MoS_2/WS_2 and $MoSe_2/WSe_2$ heterobilayers also exhibit type-II band alignments. These results are in agreement with previous findings [11, 12]. With regard to ReX_2/WX_2 (X = S, Se), for which W and Re lie in the same row in the periodic table, the CBM of WX_2 is much higher than that of ReX_2, while the VBM of WX_2 is close to that of ReX_2. More interestingly, we find that the VBM of ReS_2 is higher than that of MoS_2, while the CBM of ReS_2 is lower than that of MoS_2. Hence, MoS_2/ReS_2 heterobilayer is predicted to exhibit the type-I band alignment. This have been confirmed by our previous experiments [41]. Moreover, according to the computed band alignments, $WSe_2/MoTe_2$ and $ReSe_2/MoSe_2$ heterobilayers are likely to exhibit type-I band alignments.

In this work, we focus on $WSe_2/MoTe_2$. Our calculations show that the lattice constant of the unit cell is 3.297 Åand 3.522 Åfor WSe_2 and $MoTe_2$, respectively. To minimize the relatively large lattice mismatch of (> 6 %), a large supercell of $Mo_{54}Te_{108}$

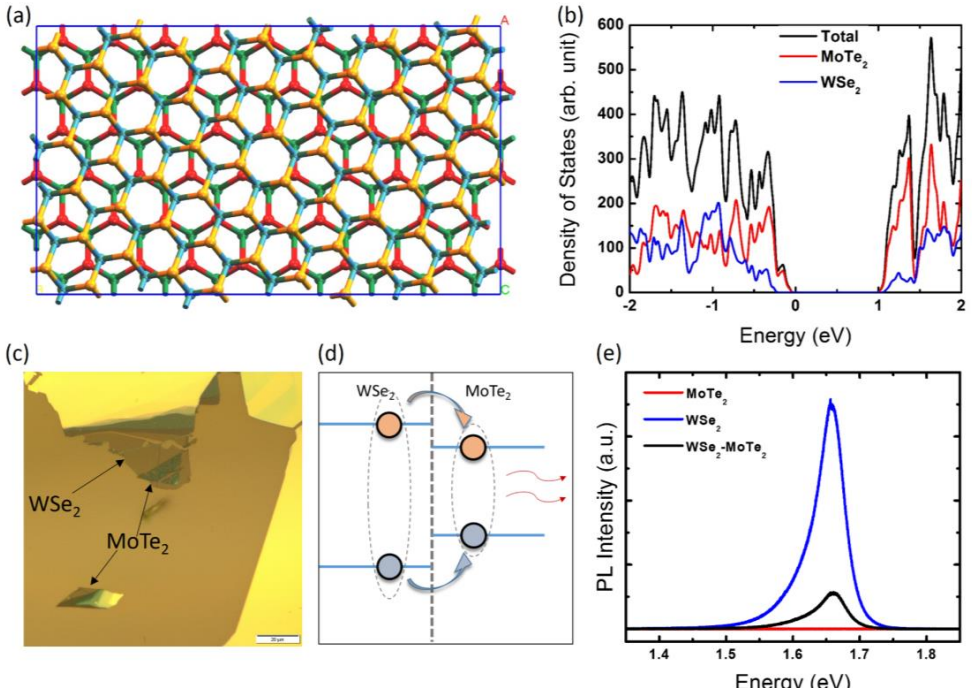

Figure 2. (a) A top view of the $WSe_2/MoTe_2$ heterobilayer. The orange, blue, red and green balls represent the W, Se, Mo and Te atoms, respectively. (b) Computed partial density of states (PDOS) of $WSe_2/MoTe_2$ heterobilayer based on the optB86b-vdW functional. The blue curves denote the DOS contributed by the WSe_2 layer while the red curves represent the DOS contributed by the $MoTe_2$ layer. The black curves show the total DOS. (c) Optical image of the $WSe_2/MoTe_2$ heterobilayer sample on a 90 nm Si/SiO_2 substrate. (d) A schematic plot of the type-I band alignment between WSe_2 and $MoTe_2$. The orange and blue circles represent electrons and holes, respectively. The schematic depicts transfer of energy from WSe_2 to $MoTe_2$ where the electrons and holes recombine, emitting near infrared photons. (e) Photoluminescence spectra of the heterobilayer and individual monolayers in the visible range. The strong quenching of the WSe_2 peak in the heterobilayer stems from energy transfer to $MoTe_2$.

is constructed from bulk $MoTe_2$ (001) with the dimension of 18.356 × 31.794 × c Å. Similarly, a large $W_{62}Se_{124}$ supercell from bulk WSe_2 (001) with the dimension of 18.298 × 31.694 × c Åwas used. With both supercells, the lattice mismatch between WSe_2 and $MoTe_2$ is now < 0.32 %. Figure 2(a) shows a top view of the relaxed $WSe_2/MoTe_2$ heterobilayer. A side view of the relaxed $WSe_2/MoTe_2$ heterobilayer is shown in Figure S2 (see supplementary material).

The computed band alignment for separated monolayer WSe_2 and monolayer $MoTe_2$ is depicted in Figure 1. It can be seen that the VBM of $MoTe_2$ is 0.14-eV higher than that of WSe_2, while the CBM of $MoTe_2$ is 0.16-eV lower than that of WSe_2. Consequently, the $WSe_2/MoTe_2$ heterobilayer exhibits the type-I band alignment. Computed partial density of states (PDOS) of the $WSe_2/MoTe_2$ heterobilayer is shown in Figure 2(b). The blue lines denote the DOS contributed by the WSe_2 layer while the red lines represent the DOS contributed by the $MoTe_2$ layer. The calculation suggests that both the VBM

and CBM are contributed by the $MoTe_2$ layer, consistent with the band alignment of $WSe_2/MoTe_2$ shown in Figure 1.

4.2. Experimental results

To confirm the theoretical prediction on the type-I band alignment of the $WSe_2/MoTe_2$ heterobilayer, we fabricated a sample and performed corresponding optical measurements. Figure 2(d) provides a schematic of the expected movement of photocarriers in this heterobilayer, due to its type-I band alignment. Excitons injected in WSe_2 transfer to $MoTe_2$ where they recombine, emitting photons (red arrows) with an energy determined by the optical bandgap of $MoTe_2$ monolayer. In the following, we present multiple pieces of experimental evidence that such transfer indeed occurs, and is highly efficient.

First, photoluminescence spectra were taken on the heterobilayer as well as both monolayer regions. As shown in Figure 2(e), the spectra of the WSe_2 monolayer and the heterobilayer both have a peak located around 1.65 eV, consistent with the A-exciton resonance in WSe_2 [42]. There is significant quenching (about 83 %) of the peak in the heterobilayer. This shows a good interface between the two layers and the existence of efficient transfer of electrons, holes, or both, from WSe_2 to $MoTe_2$. We note that the photoluminescence from $MoTe_2$ was not measured in this study since it falls out of the range of our spectroscopic system. However, several groups have reported efficient PL from monolayer $MoTe_2$ at about at 1.1 eV at room temperature and showed evidence that it is a direct semiconductor [43, 44, 45, 46, 47, 48, 49, 50].

Next, we studied the photocarrier dynamics in $MoTe_2$ monolayer. A 1.65-eV pump pulse with peak energy fluence of 8.4 μJ cm^{-2} was used to excite the $MoTe_2$ monolayer. Based on the absorption coefficient of 1×10^6cm^{-1} [43], this pump fluence corresponds to an injected photocarrier density of about 2×10^{12}cm^{-2}. The differential reflection of a 1.31-eV probe pulse was then measured for different delay times. The results are shown as the solid grey squares in Figure 3. The left and right panels of Figure 3 show the signal in short and long time ranges, respectively. Note that both the pump and the probe photon energies are significantly larger than the optical bandgap of $MoTe_2$. The rising part of the signal can be modelled by the integral of a Gaussian function with a full-width at half-maximum of 0.63 ps, as indicated by the black curve. This rising time is slightly slower than the instrument response time of about 0.4 ps, which can be attributed to the time it takes for the photocarriers to relax their energy from the injected states to the states coupled to the probe pulse. The decay of the signal after the first 1 ps can be fit by a bi-exponential function with two time constants of 2.8 and 28 ps, respectively, as shown by the red curve. The short time constant could be attributed to the energy relaxation of photocarriers from the probed state to the band edges. Previously, carrier energy relaxation times of about 0.7 and 1.8 ps at room temperature in MoS_2 have been reported [51, 52]. Considering different experimental conditions and materials, this assumption is reasonable. The long-time constant gives

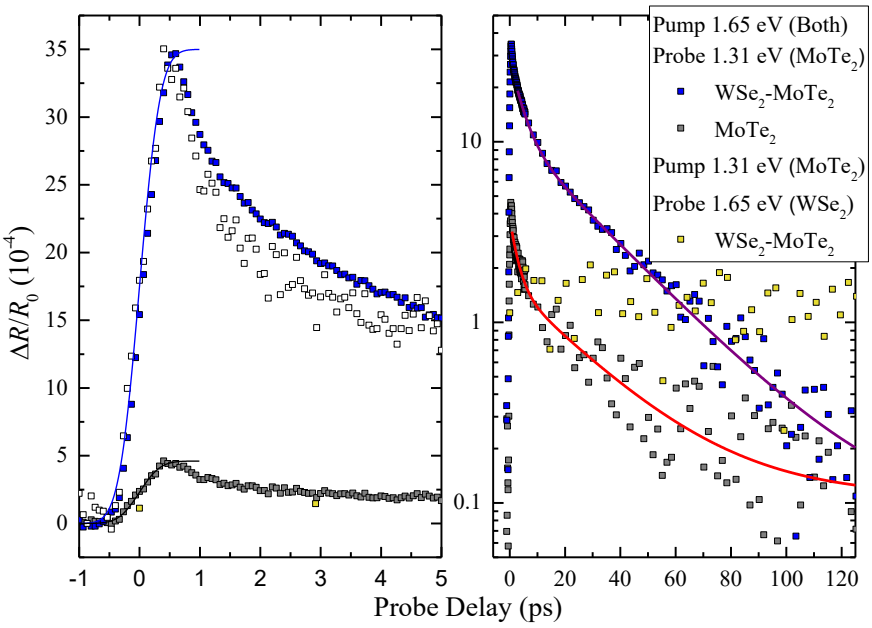

Figure 3. Differential reflection measurements using a 1.31-eV probe pulse and a 1.65-eV pump pulse. The blue squares were measured from the $WSe_2/MoTe_2$ heterobilayer and show a significantly higher signal than that measured from the isolated $MoTe_2$ monolayer (grey squares). The purple and red lines represent double-exponential fits to the data. The yellow squares represent measurements on the heterobilayer with the pump and probe switched, 1.65-eV probe and 1.31-eV pump. This is intended to probe carriers excited in $MoTe_2$ that might transfer to WSe_2, if the band alignment were type-II.

the photocarrier lifetime, which is limited by nonradiative recombination.

Using this procedure, we then measured the differential reflection signal from the heterobilayer under the same conditions. Since the optical bandgap of WSe_2 monolayer is about 1.65 eV, the pump is expected to inject photocarriers in both layers, while the 1.3-eV probe should only sense photocarriers in $MoTe_2$. The result is shown by the blue squares in Figure 3. The magnitude of the signal is about 7.5 times larger than that of $MoTe_2$. To better compare the two signals, the data from $MoTe_2$ is scaled by a factor of 7.5, as shown by the open squares. It is obvious that the two signals are very similar, except for a slightly slower initial decay. Furthermore, by bi-exponential fit (purple curve), the two time constants from the heterostructure measurement are 4.3 and 28 ps, with the long-time constant matching the $MoTe_2$ monolayer very well. The increased energy relaxation time could be attributed to the reduced electron-phonon interaction in the heterostructure due to the dielectric screening effect by the WSe_2 layer.

These features are strong evidence that both electrons and holes injected in WSe_2 transfer to $MoTe_2$, as a result of the type-I band alignment shown in Figure 2(d). First, without carrier transfer, the two measurements should yield identical results since carriers injected in WSe_2 of the heterostructure would not be sensed by the probe. The

probe only measures the carriers in $MoTe_2$ that are injected by the pump, which have the same density as the monolayer $MoTe_2$ measurement. The stronger signal observed in the heterobilayer sample is induced by photocarriers transferred from WSe_2 to $MoTe_2$. The existence of carrier transfer is also consistent with the PL quenching of WSe_2 shown in Figure 2(e). Although PL quenching of WSe_2 could also be induced by transfer of carriers to interfacial defects, the gain of carriers in $MoTe_2$ is unambiguous evidence of interlayer carrier transfer. Second, the carrier transfer occurs on a time scale shorter than the response time of the measurement. If the transfer were a slower process, the signal from the heterobilayer should have a slow rising part that matches the carrier transfer process. Third, the same decay time observed in the two samples indicate that both electrons and holes excited in WSe_2 transfer to $MoTe_2$, as dictated by the type-I alignment. If the alignment were type-II, only one type of carrier would transfer. Once the electrons and holes are separated in different layers, their recombination would be significantly suppressed, resulting in a longer lifetime of photocarriers in the heterobilayer. The extension of the carrier lifetime in type-II heterostructures has been generally observed [6, 7, 53]. The lack of the extension is a strong evidence that the alignment is not type-II.

Another key difference between the two band alignments is that, in type-II heterostructures, one type of carriers can transfer from the smaller bandgap material ($MoTe_2$ in the case) to the larger bandgap material (WSe_2), while in type-I heterostructure, neither carrier can transfer along this direction. To confirm that neither electrons nor holes transfer from $MoTe_2$ to WSe_2, we used the 1.31-eV pulse as the pump and the 1.65-eV pulse as the probe. In this configuration, photocarriers are injected in the $MoTe_2$ layer only. The 1.65-eV probe matches the A-exciton resonance of WSe_2, and hence primarily senses carriers in the WSe_2 layer. As shown by the yellow squares in Figure 3, there is no noticeable signal from the heterobilayer. In this measurement, we used a pump fluence of 16.9 μJ cm^{-2}, which is twice of what was used in the other 2 curves. If the band alignment were type-II, there would be charge separation and we would expect to observe a differential reflection signal due to either electrons or holes transferring to WSe_2 under these conditions. The absence of a signal from $MoTe_2$ can be attributed to the fact that the probe photon energy is about 0.5 eV higher than its bandgap, which is expected to have very low efficiency in probing carriers that mostly populate states below the probed states. When the same measurement was repeated on the $MoTe_2$ ML region, no signal was observed neither.

To further confirm that the increased signal observed in the heterobilayer is from photocarriers injected in WSe_2 that subsequently transferred to $MoTe_2$, we studied the dependence of this signal on the pump photon energy. Using a 1.31-eV probe, we varied the pump photon energy from 1.65 eV, the A-exciton resonance of WSe_2, to 1.55 eV. Figure 4(a) shows the differential reflection of the heterobilayer for the different pump energies. The inset shows the peak signal as a function of the pump energy. The signal increases as the pump energy moves towards the exciton resonance of WSe_2. This indicates that as more photocarriers are injected in WSe_2, subsequently the observed

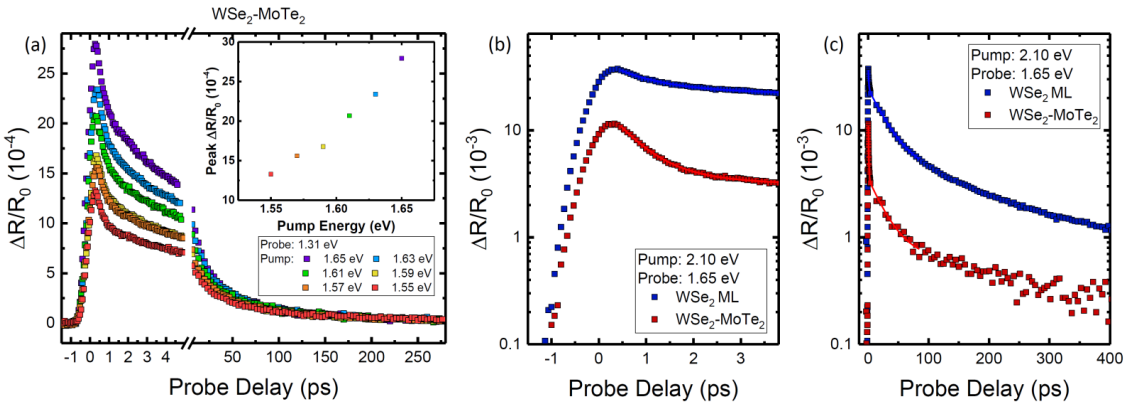

Figure 4. (a) Pump-photon-energy dependence of the differential reflection of the $WSe_2/MoTe_2$ heterobilayer measured with the 1.31-eV probe. The inset shows the peak differential reflection signal for the different pump photon energies. (b,c) Short and long scale differential reflection signal on WSe_2 monolayer (blue) and the heterostructure (red) using a 2.1-eV pump and 1 1.65-eV probe.

carrier density in $MoTe_2$ also increases. If there is no carrier transfer, the signal is expected to be independent of the pump photon energy in this range.

Finally, probing carrier dynamics in WSe_2 layer of the heterobilayer can provide further evidence of the type-I band alignment. In such a measurement, photocarriers were injected by a 2.1-eV pump in the WSe_2 monolayer and the heterobilayer with a peak fluence of 4.22 μJ cm^{-2}. From Figure 4(b), it can be seen that there is an initial fast decay in the heterobilayer that is noticeably faster than the decay in WSe_2 monolayer. Fitting each data set with a biexponential function, the initial fast decay is about 0.84 $\pm$ 0.3 ps in WSe_2 monolayer compared to 0.66 $\pm$ 0.1 ps in the heterobilayer, about a 20 % decrease. This faster decay could be attributed to carriers transferring from WSe_2 to $MoTe_2$, another indication of type-I band alignment. Figure 4(c) shows the dynamics on a longer time scale. The longer decay times are nearly identical at 33 and 29 ps in the two samples, respectively. The slow decay component account for about 30 % of the signal. This can be attributed to the carriers reside in WSe_2 because they are excited in the regions of the sample with poor interface contact. Such regions are inevitable due to foreign particles trapped between the two monolayers during the sample fabrication process. It is also important to note that the signal from the heterobilayer is smaller in magnitude than that of the isolated WSe_2 monolayer. This is evidence that a significant portion of the photocarriers transfer on an ultrafast time scale, faster than the time resolution of our system of about 300 fs.

We note that the observed transfer of electrons and holes from WSe_2 to $MoTe_2$ can be achieved via different physics mechanisms. Since both electrons and holes transfer, there is no net charge transfer. The energy transfer can be achieved by a Fröster process, where an exciton in WSe_2 recombines nonradiatively, transferring the energy for the excitation of an electron-hole pair (or exciton) in $MoTe_2$. Alternatively, the

energy transfer can be accomplished by movement of electrons and holes from WSe_2 to $MoTe_2$ in a Dexters process. It would be interesting to study the relative contributions of these processes to the observed effect; however, the results of the two processes, that is, the appearance of photocarriers in $MoTe_2$ accompanied by the annihilation of them in WSe_2, are indistinguishable in our measurements.

5. Conclusion

We have performed a joint theoretical/experimental study of a van der Waals heterobilayer with type-I band alignment. The heterobilayer is formed by monolayers of WSe_2 and $MoTe_2$. Our first-principles computation showed that both the valence band maximum and the conduction band minimum of the $WSe_2/MoTe_2$ heterobilayer reside in the $MoTe_2$ layer. Subsequent experimental study provided compiling evidence of type-I band alignment from transient absorption measurements, in consistent with our first-principles calculations. Specifically, the type-I band alignment is experimentally established by the following observations: First, when photocarriers are injected in WSe_2, we observed an instantaneous increase in carrier population in $MoTe_2$, which can only result from efficient and ultrafast carrier transfer. Second, the photocarriers lifetime in the heterobilayer is not increased from $MoTe_2$ monolayer, which rules out the layer separation of electrons and holes, and thus rules out the type-II alignment. Third, when carriers are injected in $MoTe_2$, no population of excitons is observed in WSe_2. If the alignment were type II, either electrons or holes would have transferred to WSe_2. Fourth, the population of excitons in $MoTe_2$ shows a strong dependence on the pump photon energy near the exciton resonance of WSe_2. Without carrier transfer, such dependence would not have been observed. Finally, exciton population injected in the WSe_2 layer of the heterobilayer decays rapidly, which can only be attributed to the addition population loss channel provided by the interlayer transfer. The established type-I band alignment of $WSe_2/MoTe_2$ heterobilayer facilitate its application in light emission devices. Previously, some of us have demonstrated MoS_2/ReS_2 as the first TMDC type-I heterostructure [41]. Despite of that, the introduction of $WSe_2/MoTe_2$ as another type-I heterostructure is significant. ReS_2 has a bandgap of about 1.55 eV and with low photoluminescence yield. $MoTe_2$, on the other hand, have shown strong photoluminescence in the near infrared range about 1.1 eV. Its emission performance can be enhanced by the carrier transfer from WSe_2 to $MoTe_2$. Hence, the ultrafast transfer of carriers across an atomically thin junction provides a mechanism for important optical applications in the near infrared range.

Acknowledgement

This work was supported by the US National Science Foundation (NSF) under Award No. DMR-1505852, and the National Science Foundation (NSF) through the Nebraska Materials Research Science and Engineering Center (MRSEC) (grant No. DMR-

1420645), and UNL Holland Computing Center. ML was supported by the NSFC (51472073), the Natural Science Foundation of Hebei Province (B2018209220), and the Peiyu Foundation of North China University of Science and Technology (GP201309).

References

[1] Alferov Z 2013 *Proc. IEEE* **101** 2176–2182
[2] Alferov Z I 2001 *Rev. Mod. Phys.* **73**(3) 767–782
[3] Kroemer H and Griffiths G 1983 *IEEE Elec. Dev. Lett.* **4** 20–22
[4] Geim A K and Grigorieva I V 2013 *Nature* **499** 419–425
[5] Lin Z, McCreary A, Briggs N, Subramanian S, Zhang K H, Sun Y F, Li X F, Borys N J, Yuan H T, Fullerton-Shirey S K, Chernikov A, Zhao H, McDonnell S, Lindenberg A M, Xiao K, LeRoy B J, Drndic M, Hwang J C M, Park J, Chhowalla M, Schaak R E, Javey A, Hersam M C, Robinson J and Terrones M 2016 *2D Mater.* **3** 042001
[6] Hong X, Kim J, Shi S F, Zhang Y, Jin C, Sun Y, Tongay S, Wu J, Zhang Y and Wang F 2014 *Nat. Nanotechnol.* **9** 682–686
[7] Ceballos F, Bellus M Z, Chiu H Y and Zhao H 2014 *ACS Nano* **8** 12717–12724
[8] Nourbakhsh A, Zubair A, Dresselhaus M S and Palacios T 2016 *Nano Lett.* **16**(15) 1359–1366
[9] Liao J, Sa B, Zhou J, Ahuja R and Sun Z 2014 *J. Phys. Chem. C* **118** 17594–17599
[10] Guo Z, Miao N, Zhou J, Sa B and Sun Z 2017 *J. Mater. Chem. C* **5**(4) 978–984
[11] Kang J, Tongay S, Zhou J, Li J B and Wu J Q 2013 *Appl. Phys. Lett.* **102** 012111
[12] Lu N, Guo H Y, Li L, Dai J, Wang L, Mei W N, Wu X J and Zeng X C 2014 *Nanoscale* **6** 2879–2886
[13] Andoshe D M, Jeon J M, Kim S Y and Jang H W 2015 *Elect. Mater. Lett.* **11** 323–335
[14] Kresse G and Furthmüller J 1996 *Phys. Rev. B* **54** 11169–11186
[15] Becke A D 1986 *J. Chem. Phys.* **84** 4524–4529
[16] Klimes J, Bowler D R and Michaelides A 2010 *J. Phys.: Conden. Matt.* **22** 022201
[17] Kresse G and Joubert D 1999 *Phys. Rev. B* **59**(3) 1758–1775
[18] Heyd J, Scuseria G E and Ernzerhof M 2006 *J. Chem. Physi.* **124** 219906
[19] Li M, Dai J and Zeng X C 2015 *Nanoscale* **7** 15385–15391
[20] Ceballos F, Zereshki P and Zhao H 2017 *Phys. Rev. Mater.* **1**(4) 044001
[21] Cui Q, Muniz R A, Sipe J E and Zhao H 2017 *Phys. Rev. B* **95** 165406
[22] Ceballos F and Zhao H 2017 *Adv. Funct. Mater.* **27** 1604509
[23] Arora A, Noky J, Druppel M, Jariwala B, Deilmann T, Schneider R, Schmidt R, Pozo-Zamudio O D, Stiehm T, Bhattacharya A, Kruger P, de Vasconcellos S M, Rohlfing M and Bratschitsch R 2017 *Nano Lett.* **17** 3202–3207
[24] Lamfers H J, Meetsma A, Wiegers G and de Boer J 1996 *Journal of Alloys and Compounds* **241** 34 – 39
[25] Guo H, Lu N, Wang L, Wu X and Zeng X C 2014 *J. Phys. Chem. C* **118** 7242–7249
[26] Ho C H, Huang Y S, Chen J L, Dann T E and Tiong K K 1999 *Phys. Rev. B* **60** 15766–15771
[27] Mak K F, Lee C, Hone J, Shan J and Heinz T F 2010 *Phys. Rev. Lett.* **105** 136805
[28] Splendiani A, Sun L, Zhang Y, Li T, Kim J, Chim C Y, Galli G and Wang F 2010 *Nano Lett.* **10** 1271–1275
[29] Conley H J, Wang B, Ziegler J I, Haglund R F, Pantelides S T and Bolotin K I 2013 *Nano Lett.* **13** 3626
[30] Tongay S, Zhou J, Ataca C, Lo K, Matthews T S, Li J B, Grossman J C and Wu J Q 2012 *Nano Lett.* **12** 5576–5580
[31] Jiang H 2012 *J. Phys. Chem. C* **116** 7664–7671
[32] Marzik J V, Kershaw R, Dwight K and Wold A 1984 *J. Solid State Chem.* **51** 170 – 175 ISSN 0022-4596
[33] Raybaud P, Hafner J, Kresse G and Toulhoat H 1997 *J. Phys.: Condens. Matt.* **9** 11107

[34] Friemelt K, Kulikova L, Kulyuk L, Siminel A, Arushanov E, Kloc C and Bucher E 1996 *J. Appl. Phys.* **79** 9268–9272
[35] Ho C H, Liao P C, Huang Y S, Yang T R and Tiong K K 1997 *J. Appl. Phys.* **81** 6380–6383
[36] Ho C H, Liao P C, Huang Y S and Tiong K K 1997 *Phys. Rev. B* **55** 15608–15613
[37] Tongay S, Sahin H, Ko C, Luce A, Fan W, Liu K, Zhou J, Huang Y S, Ho C H, Yan J, Ogletree D F, Aloni S, Ji J, Li S, Li J, Peeters F M and Wu J 2014 *Nat. Commun.* **5** 3252
[38] Loh G C and Pandey R 2015 *Phys. Chem. Chem. Phys.* **17**(28) 18843–18853
[39] Wolverson D, Crampin S, Kazemi A S, Ilie A and Bending S J 2014 *ACS Nano* **8** 11154–11164
[40] Jun D, Ming L and Cheng Z X *Wiley Interdisciplinary Reviews: Computational Molecular Science* **6** 211–222
[41] Bellus M Z, Li M, Lane S, Ceballos F, Cui Q, Zeng X C and Zhao H 2016 *Nanoscale Horiz.* **2** 31–36
[42] Cui Q, Ceballos F, Kumar N and Zhao H 2014 *ACS Nano* **8** 2970–2976
[43] Ruppert C, Aslan O B and Heinz T F 2014 *Nano Lett.* **14** 6231–6236
[44] Froehlicher G, Lorchat E and Berciaud S 2016 *Phys. Rev. B* **94** 085429
[45] Yang J, Lu T, Myint Y W, Pei J, Macdonald D, Zheng J C and Lu Y 2015 *ACS Nano* **9** 6603–6609
[46] Lezama I G, Arora A, Ubaldini A, Barreteau C, Giannini E, Potemski M and Morpurgo A F 2015 *Nano Lett.* **15** 2336–2342
[47] Chen B, Sahin H, Suslu A, Ding L, Bertoni M I, Peeters F M and Tongay S 2015 *ACS Nano* **9** 5326–5332
[48] Koirala S, Mouri S, Miyauchi Y and Matsuda K 2016 *Phys. Rev. B* **93** 075411
[49] Robert C, Picard R, Lagarde D, Wang G, Echeverry J P, Cadiz F, Renucci P, Högele A, Amand T, Marie X, Gerber I C and Urbaszek B 2016 *Phys. Rev. B* **94**(15) 155425
[50] Zhang K A, Zhang T N, Cheng G H, Li T X, Wang S X, Wei W, Zhou X H, Yu W W, Sun Y, Wang P, Zhang D, Zeng C G, Wang X J, Hu W D, Fan H J, Shen G Z, Chen X, Duan X F, Chang K and Dai N 2016 *ACS Nano* **10** 3852–3858
[51] Seo M, Yamaguchi H, Mohite A D, Boubanga-Tombet S, Blancon J C, Najmaei S, Ajayan P M, Lou J, Taylor A J and Prasankumar R P 2016 *Sci. Rep.* **6** 21601
[52] Nie Z, Long R, Sun L, Huang C C, Zhang J, Xiong Q, Hewak D W, Shen Z, Prezhdo O V and Loh Z H 2014 *ACS Nano* **8** 10931–10940
[53] Peng B, Yu G, Liu X, Liu B, Liang X, Bi L, Deng L, Sum T C and Loh K P 2016 *2D Mater.* **3** 025020